4126 *Biochemistry* **2009,** *48,* 4126–4138
DOI:10.1021/bi900220s

BIOCHEMISTRY
including biophysical chemistry & molecular biology
Article

Reaction Mechanism of Glutamate Carboxypeptidase II Revealed by Mutagenesis, X-ray Crystallography, and Computational Methods[†,‡]

Vojtěch Klusák,[§,#] Cyril Bařinka,[∥,#] Anna Plechanovová,[§,◇] Petra Mlčochová,[§,⊥] Jan Konvalinka,[§,⊥] Lubomír Rulíšek,*[,§] and Jacek Lubkowski*[,∥]

[§]*Institute of Organic Chemistry and Biochemistry, Gilead Sciences Research Center and IOCB, Academy of Sciences of the Czech Republic, Flemingovo nám. 2, 166 10 Praha 6, Czech Republic,* [⊥]*Department of Biochemistry, Faculty of Science, Charles University in Prague, Hlavova 2030, Praha 2, Czech Republic, and* [∥]*Macromolecular Crystallography Laboratory, National Cancer Institute at Frederick, 539 Boyles Street, Frederick, Maryland 21702* [#]*These authors contributed equally to this work* [◇] *Current address: College of Life Sciences, University of Dundee, Dundee, United Kingdom*

Received February 10, 2009. Revised Manuscript Received March 20, 2009

ABSTRACT: Glutamate carboxypeptidase II (GCPII, EC 3.4.17.21) is a zinc-dependent exopeptidase and an important therapeutic target for neurodegeneration and prostate cancer. The hydrolysis of *N*-acetyl-L-aspartyl-L-glutamate (*N*-Ac-Asp-Glu), the natural dipeptidic substrate of the GCPII, is intimately involved in cellular signaling within the mammalian nervous system, but the exact mechanism of this reaction has not yet been determined. To investigate peptide hydrolysis by GCPII in detail, we constructed a mutant of human GCPII [GCPII(E424A)], in which Glu424, a putative proton shuttle residue, is substituted with alanine. Kinetic analysis of GCPII(E424A) using *N*-Ac-Asp-Glu as substrate revealed a complete loss of catalytic activity, suggesting the direct involvement of Glu424 in peptide hydrolysis. Additionally, we determined the crystal structure of GCPII(E424A) in complex with *N*-Ac-Asp-Glu at 1.70 Å resolution. The presence of the intact substrate in the GCPII(E424A) binding cavity substantiates our kinetic data and allows a detailed analysis of GCPII/*N*-Ac-Asp-Glu interactions. The experimental data are complemented by the combined quantum mechanics/molecular mechanics calculations (QM/MM) which enabled us to characterize the transition states, including the associated reaction barriers, and provided detailed information concerning the GCPII reaction mechanism. The best estimate of the reaction barrier was calculated to be $\Delta G^{\ddagger} \approx 22(\pm 5)$ kcal·mol^{-1}, which is in a good agreement with the experimentally observed reaction rate constant ($k_{cat} \approx 1$ s^{-1}). Combined together, our results provide a detailed and consistent picture of the reaction mechanism of this highly interesting enzyme at the atomic level.

Metallopeptidases play important roles in a variety of biological processes, including angiogenesis, wound healing, and cancer metastasis (*1*,*2*).

Depending on the number of metal ions required for catalysis, metallopeptidases can be divided into two broad groups: mononuclear and cocatalytic (binuclear) enzymes. In the latter category, the two metal ions (typically Zn^{2+}) are held in position by the side chains of histidine and aspartate/glutamate residues and are in some instances additionally bridged by a water molecule (or the hydroxide anion). Although the exact roles of the individual metal ions (termed the catalytic and cocatalytic, respectively) in the reaction cycle are not fully understood, they exhibit dissimilarity in terms of binding constants, spectroscopic characteristics, and evolutionary origin (*3*−*5*).

Human glutamate carboxypeptidase II (GCPII,[1] EC 3.4.17.21) is a membrane-bound zinc-dependent exopeptidase,

[†]This project was supported by the Intramural Research Program of the National Institutes of Health, National Cancer Institute, Center for Cancer Research (C.B. and J.L.) and the Ministry of Education, Youth, and Sports of the Czech Republic (Projects 1M0508, Z40550506, and LC512). Use of the APS was supported by the U.S. Department of Energy, Office of Science, Office of Basic Energy Sciences, under Contract W-31-109-Eng-38.

[‡]The atomic coordinates and experimental diffraction amplitudes (PDB code 3BXM) have been deposited in the Protein Data Bank, Research Collaboratory for Structural Bioinformatics, Rutgers University, New Brunswick, NJ (http://www.rscb.org/).

*Corresponding authors. L.R.: tel, +420-220-183-263; fax, +420-220-183-578; e-mail, lubos@uochb.cas.cz. J.L.: tel, (301) 846-5494; fax, (301) 846-7517; e-mail, jacek@ncifcrf.gov.

[1]Abbreviations: GCPII, human glutamate carboxypeptidase II; AAP, *Aeromonas proteolytica* aminopeptidase; SGAP, *Streptomyces griseus* aminopeptidase; blLAP, bovine lens leucine aminopeptidase; PepA, *Escherichia coli* aminopeptidase A; NAAG, *N*-acetyl-L-aspartyl-L-glutamate; DFT, density functional theory; QM, quantum mechanical; MM, molecular mechanical; PDB, Protein Data Bank; B3-LYP, hybrid functional (Becke, three-parameter, Lee−Yang−Parr); PBE, Perdew−Burke−Ernzerhof functional; TS, transition state; IN, intermediate; COSMO, conductor-like screening model of solvation; PCM, polarizable continuum model; SPE, (2*S*)-2-{[(2-carboxyethyl)hydroxyphosphinoyl]methyl}pentanedioic acid.

 Published on Web 3/20/2009

a member of the M28 family of cocatalytic metallopeptidases (*6*). Other members of this family structurally related to GCPII include prokaryotic aminopeptidases from *Aeromonas proteolytica* (*7*) (AAP) and *Streptomyces griseus* (*8*) (SGAP). Human GCPII is expressed in a wide range of tissues, including brain, prostate, small intestine, and kidney (*9*−*11*). In the brain, the expression of GCPII is confined to the astrocytic plasma membrane, where it hydrolyzes endogenous *N*-acetyl-L-aspartyl-L-glutamate (*N*-Ac-Asp-Glu, also known as NAAG) with release of *N*-acetyl-L-aspartate and free glutamate (*12*), the latter being a potent excitatory neurotransmitter. In the small intestine, GCPII acts as a folate hydrolase and cleaves γ-linked glutamates from folylpoly(γ-glutamates), participating in the absorption of dietary folates (*13*). Several potent GCPII inhibitors have been shown to be neuroprotective in animal models of neurological disorders associated with high levels of glutamate, such as stroke and neuropathic pain (*14*,*15*). Additionally, GCPII is an attractive target for prostate cancer imaging, and treatment (*16*).

A better understanding of the GCPII enzymatic action has been accomplished by the determination of several GCPII crystal structures, including the unliganded form of the enzyme (*17*,*18*) and complexes with transition state analogues (*19*,*20*), glutamate as a product of *N*-Ac-Asp-Glu hydrolysis (*19*), and several glutamate mimetics/derivatives (*21*). It has been conclusively shown that there are two Zn^{2+} ions in the active site of GCPII, coordinated by two histidines (His377 and His553), two aspartates (Asp387 bridging two zinc ions and Asp453 binding one zinc in bidentate mode), and one glutamate residue (Glu425). Additionally, the oxygen atom (from either a water molecule or a hydroxide anion) bridging two zinc ions is resolved in some of the crystal structures. Last but not least, the crystallographic studies shed light on certain mechanistic aspects of the GCPII enzymatic action, such as the role of a glutarate sensor and a role of Glu424 as a putative proton shuttle (*19*). The structural results have been further complemented by the site-directed mutagenesis studies focused on the effects of mutations in both the S1 and S1′ pockets of GCPII on the K_m and k_{cat} values (*22*,*23*).

Despite the above-mentioned efforts, the reaction mechanism of GCPII is not fully understood in detail, although some information can be derived from extrapolation of the known reaction mechanism of the related AAP, for which more experimental (X-ray crystallography, kinetics, spectroscopy, and site-directed mutagenesis) and computational data are available (*24*,*25*). The general consensus concerning AAP catalytic function is that (i) the bridging oxygen is contributed by a hydroxide anion rather than a water molecule, (ii) the second shell Glu151 residue (equivalent of Glu424 in GCPII) is a proton shuttle between the bridging water molecule (which is deprotonated upon coordination to zinc ions) to the scissile peptide bond nitrogen, and (iii) the OH^- ligand must turn from the bridging to the terminal (coordinating to Zn1 only) position before it can perform a nucleophilic attack. The detailed quantum chemical investigation of the AAP reaction mechanism was also recently described (*26*). The authors carried out DFT calculations (using B3LYP functional) on the model of the active site of AAP (so-called cluster model), which was derived from an existing crystal structure of a substrate-free AAP (*24*) with a model dipeptide (Ala-Ala) docked as a substrate. The calculations indicated that the substrate is bound to the dizinc cluster via the terminal amino group rather than the peptide bond carbonyl. The bridging hydroxide is capable of performing a nucleophilic attack at the peptide bond carbonyl without the need of switching to the terminal position (i.e., coordinated to the Zn1 only), and the proton transfer from Glu151 to the nitrogen of the peptide bond was identified as the rate-determining step. The remaining steps in the reaction cycle (proton transfer from OH^- to Glu151 and C−N bond cleavage) occur through a series of several intermediates and transition states with very small reaction barriers (*26*). The role of the catalytic Zn1 ion is to stabilize the anionic tetrahedral intermediate, while cocatalytic Zn2 binds the substrate and orients the peptide bond toward the nucleophile.

The next step in understanding the catalytic properties of GCPII should be formulation of a plausible model for the mechanism of enzymatic reaction assisted by this enzyme. While the experimental data available for GCPII provide many details about the structural status of the active site at different stages of reaction, this information alone appears insufficient to formulate a detailed mechanistic view of its reaction mechanism including the structural characterization of transition state(s), plausible intermediates, and the energy profile. Therefore, in this work, we approached the problem of the mechanism of the reaction catalyzed by GCPII by combining the experimental, kinetic, and structural biology studies with theoretical calculations. We describe the construction and kinetic characterization of a hydrolytically inactive mutant of human GCPII [for the sake of simplicity and clarity of the text, we do not distinguish between recombinant human GCPII (rhGCPII) and GCPII enzymes in this report; the latter also includes transmembrane and intracellular segments (residues 1−43), whereas rhGCPII represents the hydrolytically competent extracellular part of the enzyme (residues 44−750)], GCPII(E424A). Furthermore, by solving the X-ray structure of this mutant in complex with the natural substrate, *N*-Ac-Asp-Glu, we provide the first detailed description of the Michaelis complex between GCPII and its substrate. This structure, assisted by earlier structural data on complexes between GCPII and several inhibitors as well as the product of enzymatic reaction (*19*−*21*), combined with quantum mechanical/molecular mechanical (QM/MM) calculations enabled us to propose the mechanism of substrate hydrolysis by GCPII. This included identification of the transition states and intermediate structures associated with the catalytic cycle and the calculations of energy profiles along the most favorable reaction pathway (together with free energy estimates of the transition state barrier).

MATERIALS AND METHODS

Site-Directed Mutagenesis. Site-directed mutagenesis was performed using the QuikChange site-directed mutagenesis kit (Stratagene, La Jolla, CA) according to the

manufacturer's instructions. The following oligonucleotide primers were used to introduce the E424A mutation into the pMTNAEXST (*27*) plasmid: 5′-GCTGGGATGCAGCTGAATTTGGTCTTCTTGG-3′and 5′-CCAAGAAGACCAAATTCAGCTGCATCCCAGC-3′. The presence of the E424A mutation was verified by DNA sequencing.

GCPII(E424A) Expression and Purification. GCPII (E424A) was expressed in *Drosophila* Schneider's S2 cells and purified essentially as previously described for wild-type rhGCPII (≡GCPII) (*27*). Briefly, the purification consisted of four chromatographic steps: QAE-Sephadex A50 (Pharmacia) batch chromatography, chromatography on a Source 15S column (HR10/10; Amersham Pharmacia Biotech AB, Uppsala, Sweden), affinity chromatography using lentil lectin Sepharose (Amersham Biosciences, Uppsala, Sweden), and gel permeation chromatography on a Superdex 200 column (HR16/60; Pharmacia) preequilibrated with 20 mM MOPS and 300 mM NaCl, pH 7.4. The purified protein was dialyzed against 20 mM MOPS and 20 mM NaCl, pH 7.4, and concentrated to ~9 mg/mL.

Kinetic Analysis. GCPII(E424A) (628 nM) was incubated with either 100 nM *N*-Ac-Asp-Glu [mixture of 5 nM ^{3}H-*N*-Ac-Asp-Glu (PerkinElmer, Boston, MA) and 95 nM *N*-Ac-Asp-Glu (Sigma, St. Louis, MO)] or 80 μM *N*-Ac-Asp-Glu (10 nM ^{3}H-*N*-Ac-Asp-Glu, 80 μM *N*-Ac-Asp-Glu) in 20 mM MOPS and 20 mM NaCl, pH 7.4, at 37 °C for 2 h. The reaction was terminated by the addition of an equal volume of ice-cold 200 mM potassium phosphate, pH 7.4. Released glutamate was separated from an excess of the substrate by ion-exchange chromatography and quantified by liquid scintillation.

Crystallization and Data Collection. The [GCPII (E424A)−*N*-Ac-Asp-Glu] complex was prepared by mixing the protein solution (8.7 mg/mL) with $^1/_{10}$ volume of *N*-Ac-Asp-Glu (Sigma; 20 mM in water). Hanging drops were set up by combining 2 μL of GCPII(E424A)−*N*-Ac-Asp-Glu and an equal volume of the reservoir solution containing 33% (v/v) pentaerythritol propoxylate PO/OH 5/4 (Hampton Research), 0.5% (w/v) PEG 3350, and 100 mM Tris-HCl, pH 8.0. The crystals usually appeared after 1 day and grew to a final size of approximately 0.4 × 0.4 × 0.2 mm within following week. The crystals were taken from the droplets and frozen directly in a stream of liquid nitrogen. Diffraction data were collected from a single crystal at 100 K using synchrotron radiation at the SER-CAT beamline 22-BM at the Advanced Photon Source (Argonne, IL) with the X-ray wavelength of 1.00 Å. The images were recorded on a MAR225 CCD detector (MAR-Research, Hamburg), and the diffraction intensities were integrated and scaled using the HKL2000 software package (*28*).

Structure Determination and Refinement. Crystals of the [GCPII(E424A)−*N*-Ac-Asp-Glu] complex belong to the space group *I*222 with cell dimensions a = 102.1 Å, b = 129.8 Å, and c = 159.6 Å and are isomorphous with previously reported crystals of ligand-free GCPII (*18*). Consequently, the model of ligand-free GCPII (RSCB PDB code 2OOT) was used as a template for initial structure determination. The structure was then refined and manually rebuilt using the programs Refmac5 (*29*) and Xtalview (*30*), respectively. During refinement, ~1.2% of randomly selected reflections were set aside for cross-validation (R_{free}). The quality of the final model was evaluated using the program PROCHECK (*31*). Ramachandran analysis of the final model classifies all residues but one, Lys207, as having either favorable or allowed conformations. Furthermore, all atoms of Lys207 are well-defined by the electron density peaks despite the fact that the residue falls into the disallowed region of the Ramachandran plot. The final statistics for data collection and structure refinement are shown in Table 1.

THEORETICAL CALCULATIONS

QM/MM Procedure. All QM/MM calculations were carried out with the ComQum program (*32*). In the current version, the program uses Turbomole 5.7 (*33*) for the QM part and AMBER 8 (University of California, San Francisco, CA) with the Cornell force field (*34*) for the MM part. In this approach, the protein and solvent are split into three subsystems: The QM region (system 1) contains most of the atoms relevant for the chemical process under consideration (i.e., the active site and its nearest vicinity) and is relaxed by QM/MM forces. System 2 consists of all residues within 6 Å of any atom

Table 1: Data Collection and Refinement Statistics

Data Collection Statistics	
wavelength (Å)	1.00
space group	*I*222
unit cell parameters *a*, *b*, *c* (Å)	102.1, 129.8, 159.6
resolution limits (Å)	20.0−1.70 (1.76−1.70)[a]
no. of unique reflections	113478 (11035)
redundancy	8.3 (6.5)
completeness (%)	98.8 (96.9)
$I/\sigma I$	14.6 (3.5)
R_{merge}	0.105 (0.393)
Refinement Statistics	
resolution limits (Å)	15.0−1.70 (1.75−1.70)
no. of reflections in working set	110478 (7745)
no. of reflections in test set	1374 (109)
R/R_{free}	0.184 (0.266)/0.213 (0.292)
total no. of non-H atoms	6350
no. of ions (Zn^{2+}, Ca^{2+}, Cl^-)	4
no. of water atoms	496
average *B*-factor (Å^2)	
protein atoms	29.2
N-Ac-Asp-Glu	26.7
waters atoms	38.4
rms deviations	
bond lengths (Å)	0.021
bond angles (deg)	1.87
Ramachandran plot (%)	
most favored	90.0
additionally allowed	9.3
generously allowed	0.5
disallowed	0.2 (Lys207)
missing residues	44−54, 654−655

[a] Values in parentheses correspond to the highest resolution shells.

in system 1 and is relaxed by a full MM minimization in each step of the QM/MM geometry optimization. Finally, system 3 contains the remaining part of the protein and surrounding solvent molecules and is kept fixed at the original (crystallographic) coordinates. In the quantum chemical calculations, the QM system is represented by a wave function, whereas all of the other atoms are represented by an array of partial point charges, one per atom, taken from Amber libraries. Thereby, the polarization of the quantum chemical system by the surroundings is included in a self-consistent manner. In the MM calculations for the QM/MM forces and energies, all atoms are represented by the Amber force field. When there is a bond spanning the boundary of systems 1 and 2 (a junction), the quantum region is reduced to hydrogen atoms, the positions of which are linearly related to the corresponding carbon atoms in the full system (the hydrogen link approach) (*32*). In order to avoid overpolarization of the quantum system, point charges on the atoms in the MM region bound to the junction atoms are omitted, and the remaining charges on the truncated amino acid are adjusted to keep the fragment neutral. The actual charges used for all atoms can be found in the sample PDB file in the Supporting Information (last column). The total energy is calculated as

$$E_{\mathrm{tot}} = E_{\mathrm{QM}} + E_{\mathrm{MM123}} - E_{\mathrm{MM1}} \quad (1)$$

E_{QM} is the QM energy of the quantum system truncated by hydrogen atoms in the field of the surrounding point charges, but excluding the self-energy of the point charges. E_{MM1} is the MM energy of the quantum system, still truncated by hydrogen atoms but without any electrostatic interactions. Finally, E_{MM123} is the classical energy of all atoms in the system with original atoms at the junctions and with the charges of the quantum system set to zero (to avoid double counting of the electrostatic interactions).

The Protein (GCPII) Setup. All structural models used in QM/MM calculations were based on the 2.0 Å structure of human GCPII [PDB code 2C6C, structure with GPI-18431 (*S*)-2-(4-iodobenzylphosphonomethyl)pentanedioic acid, a transition state analogue]. This structure was selected because it had the highest resolution of available GCPII structures at the time QM/MM calculations were started.

Prior to QM/MM modeling, three missing loops (accounting for total of 12 amino acids and located on the protein surface, ~10 Å from the active site) were modeled based on a low-resolution GCPII structure (PDB code 1Z8L) (*17*). This modeling task can, of course, slightly increase the uncertainty in the calculated properties; however, to study the conformational changes of the loop is well beyond the scope of this work and beyond capabilities of QM/MM methods. Then, a total of ~100 atoms, representing the side chains that were missing in the crystal structure, were added using standard Amber libraries. Finally, hydrogen atoms were added to the composite model, and the protein molecule was solvated in a truncated octahedral box. The positions of all hydrogen atoms, all non-hydrogen atoms added as described above, and solvent water molecules were subsequently optimized during a 180 ps simulated annealing (i.e., molecular dynamics simulation, using constant volume and periodic boundary conditions) followed by a conjugate gradient energy minimization of their positions. We assumed the standard protonation states at pH 7 for all amino acids. For the histidine residues, the protonation status was assigned based on a detailed study of the hydrogen bond network around the residue and the solvent accessibility. Thus, histidines 82, 347, 377, 553, and 573 were assumed to be protonated on the Nδ1 atom; histidines 111, 124, 295, 396, 475, 689, and 697 on the Nε2 atom; and histidines 345 and 618 on both nitrogens. Finally, two QM systems were defined: smaller (Q1, 175 atoms) for the geometry optimization (including transition states) and larger (Q2, 217 atoms) for the final single point calculations at the DFT (B3-LYP)/def2-TZVP level. The QM system (Q1) consisted of the following atoms (residues): the substrate (*N*-Ac-Asp-Glu); two zinc ions; the bridging H_2O/OH^-; and the side chains of Arg210, His377, Asp387, Glu424, Glu425, Asp453, Arg536, Tyr552, His553, and Tyr700. For residues Asn519 and Asp520 all atoms were included, and this fragment was capped by the carbonyl group of Gly518 at the N terminus and by the nitrogen and Cα of Phe521 at the C terminus (see also Figure S1, Supporting Information). For the final single point calculations (Q2) the following residues were added: side chains of Asn257, Ser431, Arg534, and Lys699 and three water molecules.

Quantum Chemical Calculations. All quantum chemical calculations were performed at the density functional theory (DFT) level. Geometry optimizations were carried out at the Perdew−Burke−Ernzerhof (PBE) level (*35*). The DFT/PBE calculations were expedited by expanding the Coulomb integrals in an auxiliary basis set: the resolution-of-identity (RI-J) approximation (*36*). The def2-SVP basis set was employed for all atoms (*37*). The single-point energies were then calculated using the B3-LYP method (*38*) as implemented in Turbomole 5.8. For these calculations the def2-TZVP basis set was employed for all atoms (*37*). For reference reactions in solvent, the coupled cluster (CC2) method was employed using aug-cc-pVDZ (*39*) and aug-cc-pVTZ (*40*) basis sets. To account for solvation effects, the conductor-like screening model (COSMO) method (*41*) was used with the dielectric constant corresponding to water ($\varepsilon_r = 80$). The Gibbs free energy was then calculated as a sum of the following contributions:

$$G = E_{\mathrm{el}} + G_{\mathrm{solv}} + E_{\mathrm{ZPE}} - RT \ln(q_{\mathrm{trans}} q_{\mathrm{rot}} q_{\mathrm{vib}}) \quad (2)$$

where E_{el} is the *in vacuo* energy of the system, G_{solv} is the solvation free energy, E_{ZPE} is the zero-point energy, and $-RT \ln(q_{\mathrm{trans}}\, q_{\mathrm{rot}}\, q_{\mathrm{vib}})$ accounts for the entropic terms and the thermal correction to the enthalpy obtained from a frequency calculation at 298 K at 101.3 kPa (1 atm) using the ideal gas approximation.

Transition State Optimizations and Calculations of Entropic Contributions. The full implementation of the QM/MM procedure involves a complete scan of four coupled integrals of freedom ($N_{\mathrm{pep}}-H_{\mathrm{Glu424}}$, $C_{\mathrm{pept}}-O_{\mathrm{OH}}$, $H_{\mathrm{OH}^-}-O_{\mathrm{Glu424}}$, and $C_{\mathrm{pept}}-N_{\mathrm{pept}}$ stretches). Due to the

lack of analytical expression for second derivatives, to make these calculations feasible, we utilized carefully selected and monitored one-dimensional scans (applying a harmonic force as a restraint to the distance scanned). The structures of the approximate QM/MM transition states are close to the intermediate structure. Hence the simplest way to obtain the structures of transition states (TS) is to start from the intermediate structure. The first TS (TS1), situated at the reaction coordinate between the reactant structure and the intermediate structure, was localized by scanning the $C_{pept}-O_{OH^-}$ distance. The second transition state (TS2), located between the intermediate structure and the product, was found by scanning the $N_{pept}-H_{Glu424}$ distance. For TS1 and TS2 the approximate QM/MM TS can be defined as the last structure along the reaction coordinate (step size of 0.05 Å) before the point from which the unrestrained QM/MM optimization leads the structure into the reactant (from TS1) or the product (from TS2) region. Consequently, the approximate TS structure is the highest point of an energy profile along the restrained coordinate. To verify the nature of the transition state, the QM region in the geometry corresponding to the approximate QM/MM TS was further optimized *in vacuo*. Subsequently, normal mode analysis was carried out on these QM models to estimate the entropic contributions to the reaction barrier and to verify the TS by the presence of a single imaginary frequency.

RESULTS

The E424A Mutation Results in a Complete Loss of Enzymatic Activity. The GCPII(E424A) mutant was heterologously overexpressed in *Drosophila* S2 cells and purified to near homogeneity from the conditioned media. Efficient secretion into the growth media, with a yield of approximately 1 mg/L, suggested the correct fold of the protein (later confirmed by X-ray analysis). Kinetic analysis of the E424A mutant, with *N*-Ac-Asp-Glu as a substrate, reveals a complete loss of hydrolytic activity, with a value of $k_{cat} < 0.001\ s^{-1}$ (data not shown).

The Architecture of the Substrate Binding Site Is Not Altered by the E424A Mutation. The interpretation of the results from kinetic analysis of the mutant might be obscured by accompanying conformational changes within the protein molecule. To monitor these effects and to provide further insight into the mechanism of substrate hydrolysis by GCPII, we determined the crystal structure of the [GCPII(E424A)−*N*-Ac-Asp-Glu] complex by difference Fourier methods and refined it to 1.70 Å resolution, with crystallographic parameters of $R = 0.184$ and $R_{free} = 0.213$ (Table 1). Our results show that the overall fold of the mutant is indistinguishable from that of the wild-type enzyme as documented by rms deviations of 0.45, 0.26, and 0.17 Å for ligand-free GCPII (PDB code 2OOT), the [GCPII−glutamate] (PDB code 2C6G), and [GCPII−SPE] (PDB code 3BHX) complexes, respectively (cf. Figure S8C, Supporting Information). More importantly, the architecture of the substrate binding site of GCPII(E424A) is virtually identical to the arrangement of the corresponding part of the wild-type enzyme. In the [GCPII(E424A)−*N*-Ac-Asp-Glu] complex the side chain of Glu424 (mutated to alanine) is replaced by two water molecules, and the waters occupy positions similar to those of the γ-carboxylate oxygens of Glu424 in the wild-type structure (Figure 1).

GCPII/N-Ac-Asp-Glu Interactions in the Substrate Binding Cavity. The β-carboxylate group of the substrate's Asp is engaged in ionic interactions with the guanidinium groups of Arg534 (2.9 Å) and Arg536 (3.1 Å) and forms a hydrogen bond to Asn519 Nδ2 (3.0 Å) and two water molecules (2.7, 2.7 Å). The carbonyl oxygen of the acetyl group interacts with the side chains of Arg536 (O···Nη2, 2.7 Å), Asp453 (O···Oδ2, 3.0 Å), and Asn519 (O···Nδ2, 3.1 Å), while the methyl group extends into a pocket delineated by the side chains of Ile386, Asp387, Ser454, Glu457, and Tyr549 (see Figure S8B, Supporting Information).

The C-terminal glutamate of the substrate is placed in the S1′ pocket of GCPII in a manner that approximately replicates the binding of free glutamate (a reaction product, PDB code 2C6G) or the glutarate moiety of a phosphopeptide transition state mimetic (*19*,*20*) (PDB code 3BHX, Figures S2 and S8C). However, there is a noticeable difference in the position of the carbonyl and amide groups of the scissile peptide bond of *N*-Ac-Asp-Glu and the corresponding atoms of the phosphopeptide transition state mimetic or reaction product. Transition from a substrate featuring the planar peptide bond to a reaction transition state with sp^3 hybridization at the carbonyl carbon is achieved by an approximately 1 Å shift of the carbonyl carbon with concomitant positional adjustments of the GCPII active site residues and Zn^{2+} ions (Figure S2, Supporting Information). These experimental observations are also seen during the QM/MM calculations of the GCPII reaction cycle, which suggest similar structural changes for the transition state structure during substrate hydrolysis by GCPII.

In the QM/MM optimized model (Figure 2), the enzyme/substrate interaction pattern in the S1 and S1′ pockets is in a very good agreement with the one described for the crystal structure of the [GCPII (E424A)−*N*-Ac-Asp-Glu] complex. Additionally, the interactions of the scissile peptide bond could be summarized as (i) a weak interaction of the carbonyl oxygen with Zn1 ($R_{Zn-O} = 2.6$ Å in the X-ray structure and 3.5 Å in the QM/MM equilibrium structure), (ii) a presence of the hydrogen bond between the carbonyl oxygen and the Tyr552 hydroxyl group (O···O distance of 2.6 Å in both structures), with the latter being polarized by Arg210 (we assume that this polarization considerably strengthens the $O_{pept}\cdots H-O_{Tyr552}$ hydrogen bond, which has an important effect on catalysis), and (iii) formation of the H-bond between the N−H group of the scissile peptide and the Gly518 carbonyl oxygen (N···O distance of 2.9 Å in the X-ray structure and 3.2 Å in the QM/MM model).

GCPII-Catalyzed N-Ac-Asp-Glu Hydrolysis: Definition of the Michaelis Complex. In the [GCPII(E424A)−*N*-Ac-Asp-Glu] crystal structure (Figure 2), the active site Zn^{2+} ions are positioned at a distance of 3.3 Å with the bridging oxygen placed symmetrically in between

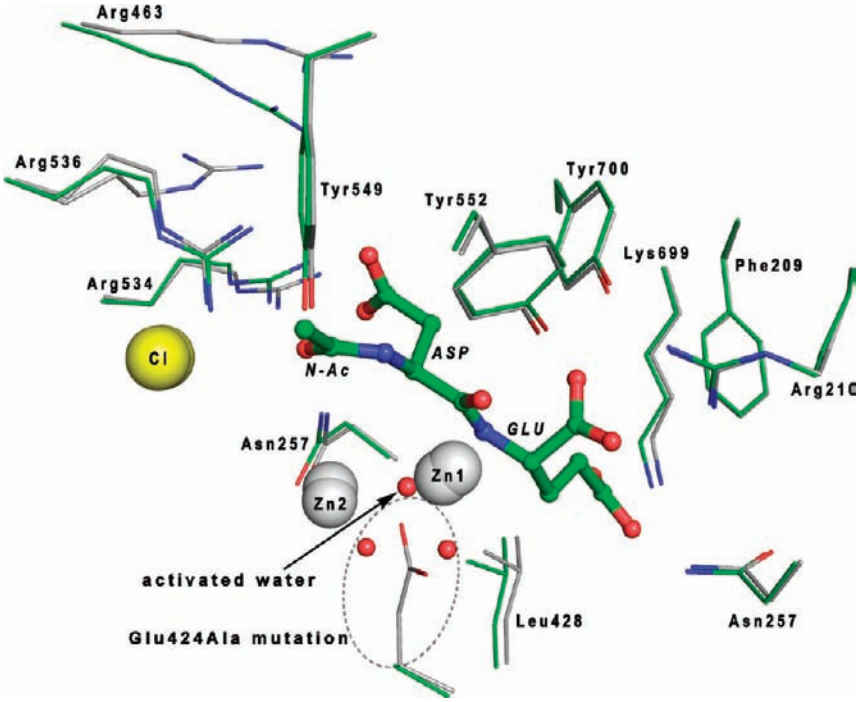

FIGURE 1: Structural comparison of the substrate binding cavity of wild-type GCPII and the GCPII(E424A) mutant. The structure of the [GCPII (E424A)−*N*-Ac-Asp-Glu] complex (carbon atoms colored green) was superimposed on the structure of the wild-type [GCPII−inhibitor(SPE)] complex (carbon atoms colored gray; the inhibitor was omitted for clarity; PDB code 3BHX) (*23*). Protein residues are depicted as thinner sticks, the active site bound NAAG is in ball-and-stick representation, and Zn^{2+} and Cl^{-} ions are shown as gray and yellow spheres, respectively. Note the presence of two water molecules (red spheres within dashed oval) at the approximate positions of the "missing" Glu424 γ-carboxylate group. The picture was generated using Pymol v0.99 (www.pymol.org).

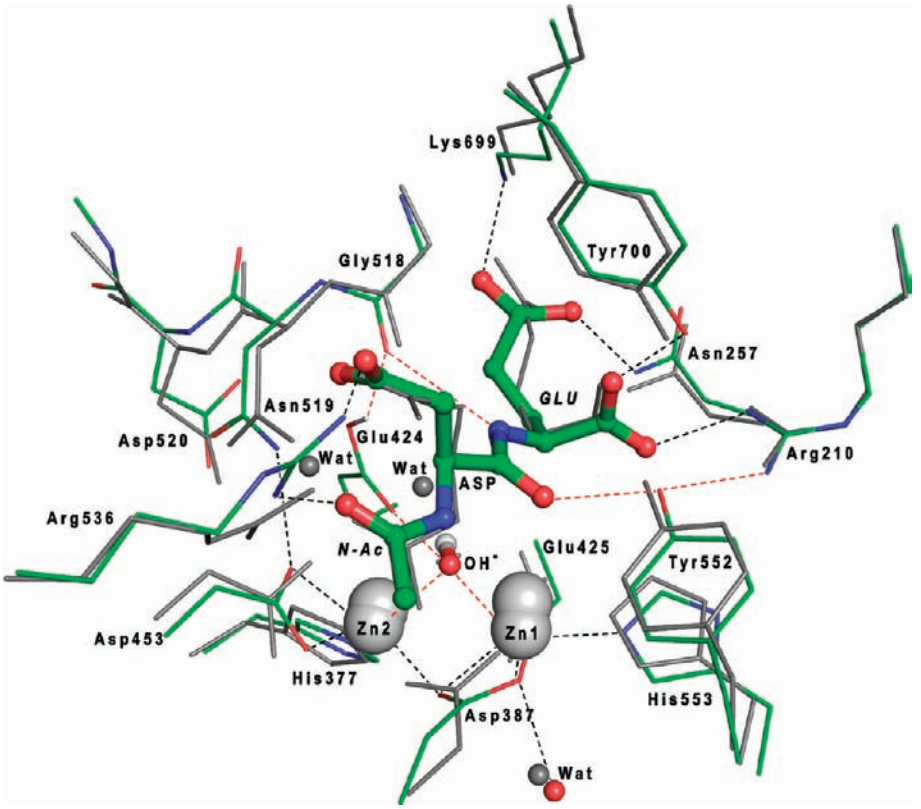

FIGURE 2: Superposition of the GCPII(E424A) X-ray structure and the QM/MM equilibrium structure of the Michaelis complex of substrate (*N*-Ac-Asp-Glu) in the active site of GCPII. The X-ray structure is shown in gray. Protein residues are depicted as thin sticks, the active site bound *N*-Ac-Asp-Glu is presented in ball-and-stick representation, and Zn^{2+} are shown as gray spheres. The important noncovalent interactions are shown as dotted lines (the interactions discussed in the text are in red).

them at a distance of 2.0 Å from each Zn^{2+}. Likewise, the active site Zn^{2+} ions in the optimized QM/MM model (Figure 2) are placed at a distance of 3.3 Å with the bridging hydroxide placed symmetrically in between them (both Zn−O distances are 2.2 Å). Our calculations indicate that the activated water molecule loses one of its

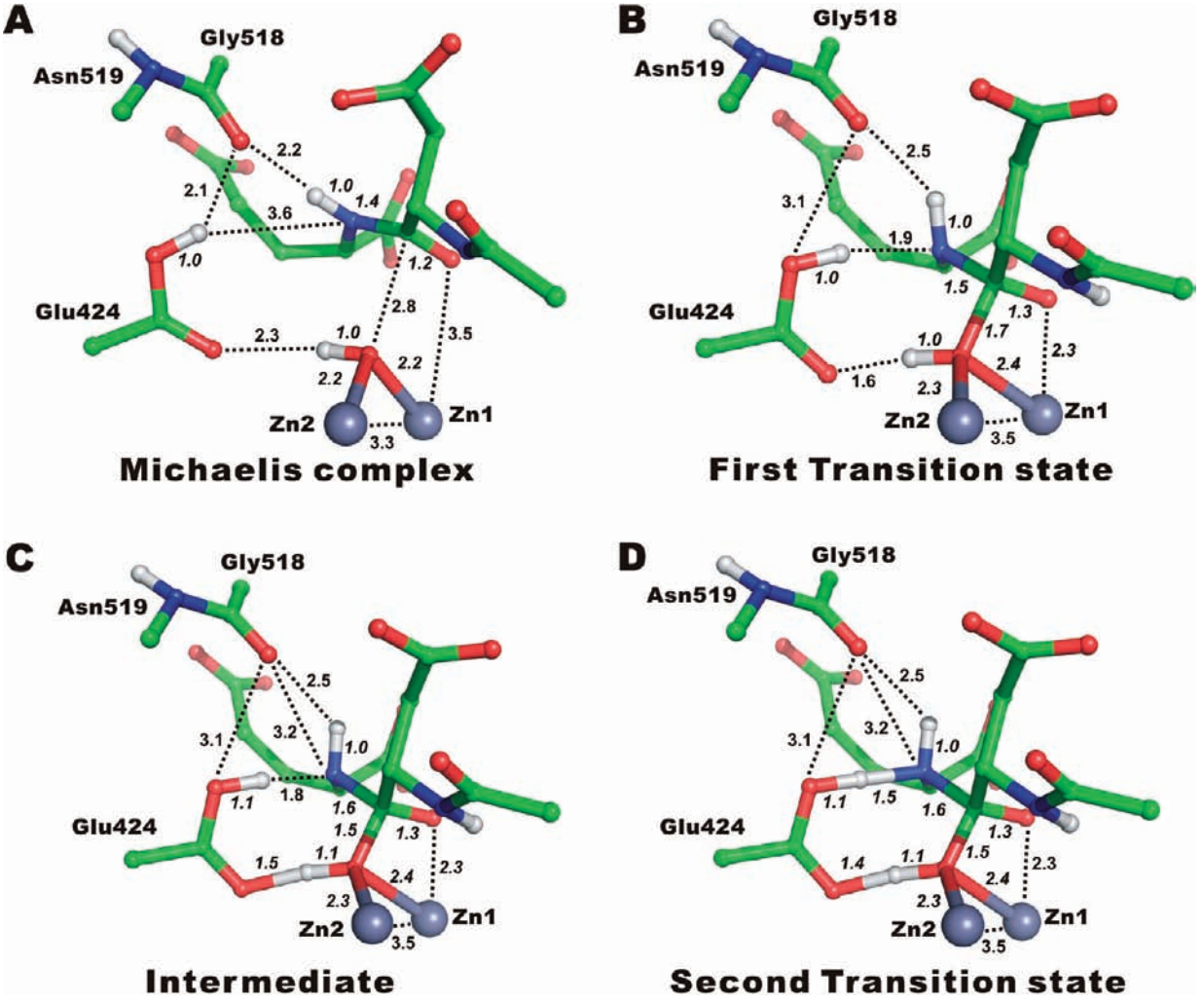

FIGURE 3: The QM/MM equilibrium structures of (A) the Michaelis complex (substrate bound in the active site), (B) the first transition state (TS1), (C) the reaction intermediate, and (D) the second, rate-determining, transition state (TS2) leading to the products. Important bond lengths and other interatomic distances are shown in italic and regular font, respectively.

protons as soon as it bridges the two Zn^{2+} ions. We did not identify any stable structure corresponding to the $Zn^{2+}-(H_2O)-Zn^{2+}$ protonation state. These observations are supported by comparing the Zn−O distances in GCPII crystal structures with standard $Zn-H_2O$ and $Zn-OH^-$ distances (2.2−2.4 and 1.8−2.0 Å, respectively) found in the Cambridge Structural Database (CSD) and with those obtained by computational methods (*42*,*43*). Similar conclusions were reported for AAP (*24*,*44*,*45*), a dizinc enzyme with an almost identical first coordination shell.

Several potential protonation sites for the leaving proton were identified and subjected to QM/MM energy minimization. These sites include the oxygen atom of the substrate scissile peptide bond and both γ-carboxylate oxygens of Glu424 (in several conformations of this residue). The calculations identified the Glu424 γ-carboxylate as the most likely proton acceptor. In the QM/MM minimized model, the Glu424 side chain attains the conformation in which the carboxylic oxygen interacts with the bridging OH^- moiety (Oε1···H−O hydrogen bond of 3.2 Å) and at the same time the hydroxyl part of the carboxylic group serves as an H-bond donor, interacting with the Gly518 backbone carbonyl group: d(Oε2−H(Glu424)···O(Gly518)) = 2.9 Å (see Figure 2).

GCPII Reaction Cycle: Reaction Intermediates. In the conformational search for a putative reaction intermediate, we identified a local minimum which is 26.1 kcal·mol^{-1} higher in energy than the reactant structure (at the QM(B3LYP/def2-TZVP)/MM level). The structure corresponding to this minimum (shown in Figure 3C) is considered by us as the key structure in the whole reaction cycle, since it lies between two small activation barriers (transition states TS1 and TS2, depicted in panels B and D of Figure 3) on the pathway from the reactant to the product. The important structural characteristics of the reaction intermediate include (i) the elongated Zn−Zn distance (3.5 Å), (ii) a newly formed C−O bond between the carbon atom of the *N*-Ac-Asp-Glu peptide bond and the oxygen atom from the bridging hydroxide, (iii) stabilization of the *N*-Ac-Asp-Glu carbonyl oxygen by Zn1 and Tyr552, and, the most importantly, (iv) the repositioning of the protonated Glu424 OH group. In the Michaelis complex (Figure 3A), the Glu424 hydroxyl group originally points to the carbonyl oxygen of Gly518, whereas during the reaction it rotates slightly and stabilizes the pyramidal nitrogen atom of *N*-Ac-Asp-Glu via a newly formed hydrogen bond. Stabilization of the pyramidal nitrogen is in turn essential for the stability of the tetrahedral

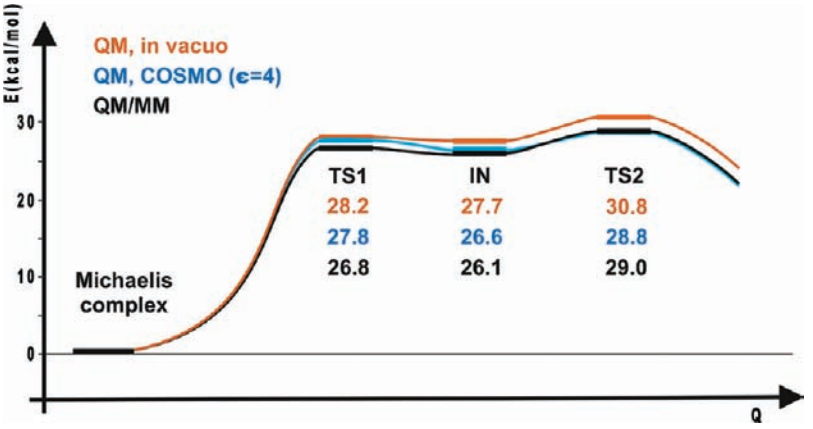

FIGURE 4: The approximate free energy profile along the reaction pathway of *N*-Ac-Asp-Glu hydrolysis catalyzed by human GCPII. QM is the energy of the system (cluster model) *in vacuo* or is calculated using the polarized continuum model (QM, COSMO), whereas QM/MM is the full QM/MM energy, calculated at the QM(B3LYP/def2-TZVP) level. All structures were generated using the QM/MM method (see text).

carbon intermediate (with the C−O bond being already formed) and is a key feature of the catalytic cycle. According to our QM/MM calculations, direct nucleophilic attack of the bridging hydroxide moiety without an additional interaction stabilizing the pyramidal nitrogen is unlikely, since after lifting a restraint to the bonding distance between the peptide bond carbon and the oxygen of the bridging hydroxide, the putative tetrahedral intermediate dissociates.

It should also be noted that we extensively searched for reaction pathways associated with the nucleophilic attack of the hydroxide moiety bound only to one zinc ion (terminal OH). We identified two energy minima corresponding to tetrahedral intermediates associated with this pathway. However, when compared to the energy of the initial reactant structure, the QM/MM energies of these intermediates are too great for the reaction to proceed (see Supporting Information for the structures and QM/MM energies of these conformers). Consequently, we assume that such a reaction pathway is unlikely in the case of the *N*-Ac-Asp-Glu hydrolysis by GCPII.

GCPII Reaction Cycle: Transition States. The structures of TS1 and TS2 are depicted in panels B and D of Figure 3, respectively. The most important structural features of these transition states are similar to those of the reaction intermediate. In TS1 (Figure 3B), the hydrogen from the Glu424 hydroxyl group is already in the near-attack conformation, with an H−N distance of 1.9 Å. As compared to the Michaelis complex, the Zn−Zn distance is elongated by ~0.2 Å to 3.5 Å, and the peptide oxygen is stabilized by Zn1 (R−Zn−O = 2.3 Å). In the second, probably the rate-determining, transition state (leading to the product state), the elongation of the hydrolyzed C−N bond (1.6 Å) is apparent, and the reaction is completed by a proton transfer from the Glu424 hydroxyl to the peptide bond nitrogen, a proton transfer from the OH^- moiety to Glu424, and the cleavage of the scissile peptide.

GCPII Reaction Cycle: Product Formation. Following the second transition, the system moves toward the products. The addition of a water molecule replacing the bridging hydroxide moiety (which was used in the hydrolytic reaction) results in the spontaneous dissociation of *N*-Ac-Asp (one of the products) from the active site. QM/MM calculations suggest that the *N*-Ac-Asp moiety is pulled from the active site presumably by several charged arginine residues (Arg463, Arg511, Arg534, Arg536) located in the exit channel of the enzyme (*19*). Since QM/MM is not a suitable technique for describing large-scale movements in protein structures, once the *N*-Ac-Asp approaches the borders of the QM system, QM energy starts to diverge, preventing us from obtaining a reliable energy comparison of the reactant and product states. The glutamate moiety (second product) remains tightly bound in the active site, adopting the conformation which is quite similar to that found in a crystal structure of the GCPII/Glu complex. After removal of the dissociating *N*-Ac-Asp moiety from the QM/MM calculations and its replacement by two water molecules, the QM/MM optimization results in a structure virtually identical to the experimental GCPII/Glu complex (*19*). The superposition of these three structures (GCPII/Glu crystal structure and the two QM/MM models: one with the cleaved *N*-Ac-Asp-Glu and the second with *N*-Ac-Asp replaced by two water molecules, i.e., QM/MM GCPII/Glu model) is shown in Figure S3, Supporting Information. We consider this finding (the dissociation of *N*-Ac-Asp and binding of Glu moiety) as additional validation of the reaction mechanism, proposed here.

GCPII Reaction Cycle: Energetic Considerations. The free energy profile of the GCPII-catalyzed *N*-Ac-Asp-Glu hydrolyis is shown in Figure 4.

At all three levels of approximation (QM, QM/PCM, QM/MM), both transition states are associated with activation barriers that are energetically very close to each other (i.e., $\triangle G^{\ddagger}$(TS1) ≈ $\triangle G^{\ddagger}$(TS2)). We showed that the simplest QM model (single point energy at the corresponding QM/MM optimized geometry) predicts the highest activation barrier (TS2) of ~31 kcal·mol^{-1}. The more complex QM/PCM(COSMO) model (i.e., QM calculations using a polarized continuum dielectric to account for bulk effects at the QM/MM geometries) already predicts stabilization of the intermediate structure and transition states by 0.4−2 kcal·mol^{-1} which is also reproduced by the QM/MM calculations. In order to benchmark the value of QM(B3LYP) energy, we carried out the reference coupled cluster (CC2) calculations for

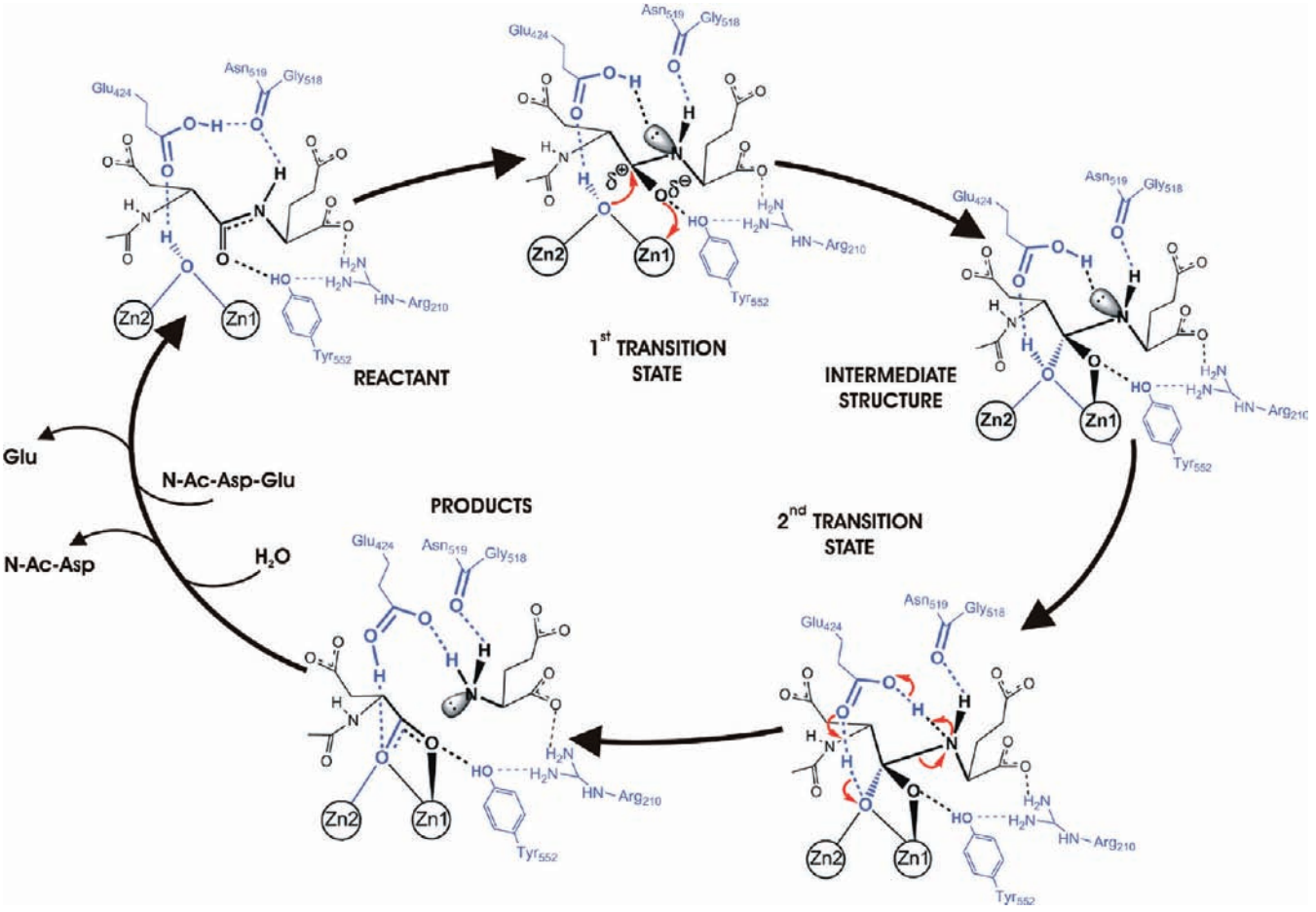

FIGURE 5: The GCPII reaction cycle. This cycle depicts important steps/structures throughout the reaction pathway. The suggested reaction mechanism was obtained by QM/MM calculations. It is fully consistent with the crystal structure of the substrate bound in the active site of the E424A mutant of GCPII reported here as well as with the structures of the transition state analogue, and enzyme−product complexes reported previously (*19*,*20*).

the two model reactions, hydrolysis of model *N*-Ac-Ala-Ala dipeptide and the substrate (*N*-Ac-Asp-Glu). In both cases, the calculated DFT(B3LYP) activation barriers are ~9 kcal·mol^{-1} higher than the reference values (Table S1 and Figure S5, Supporting Information). Therefore, it seems justified to apply the $\triangle E_{CC}$ = 9 kcal·mol^{-1} correction to values calculated by the QM(DFT/B3LYP) or QM(DFT/B3LYP)/MM methods to obtain a more reliable value of the reaction barrier. By applying this correction to the calculated $\triangle E^{\ddagger}_{QM/MM}$(TS2) activation barrier of 29 kcal·mol^{-1}, the activation barrier of the *N*-Ac-Asp-Glu hydrolysis ($\triangle E^{\ddagger}_{QM(CC)/MM}$) equals 20 kcal·mol^{-1} with the formation of TS2 being the rate-determining step, though only by a very small margin (with respect to the TS1).

To account for the entropic terms, zero-point energy contribution, and verify the nature of the approximate transition state (i.e., the existence of a single imaginary frequency), we optimized structures of TS1 and TS2 obtained by QM/MM calculations *in vacuo*. These calculations resulted in a model structure that is quite similar to the QM region of the QM/MM calculation (see Figure S4, Supporting Information for the superposition of the TS2 structures and the Supporting Information for the corresponding Cartesian coordinates of both TS1 and TS2 *in vacuo*). The *in vacuo* TS2 is characterized by one imaginary frequency of *i*225 cm^{-1} corresponding to the concerted transfer of the first proton from Glu424 to the N_{pept} atom, a transfer of the second proton from the bridging OH^- to Glu424, and cleavage of the C−N bond. The frequency calculation also allowed us to estimate the entropy contribution ($-T\triangle S$ term), which was calculated to be ~2 kcal·mol^{-1}. In summary, our best estimate of the activation barrier is $\triangle G^{\ddagger}_{calc}$ = 22 kcal·mol^{-1} with an estimated error of at least 5 kcal·mol^{-1} (arising by the neglect of dynamical sampling and uncertainty in entropic terms). This value ($\triangle G^{\ddagger}_{calc}$) is in a good agreement with the reported k_{cat} value of 1 s^{-1} (corresponding to $\triangle G^{\ddagger}_{exp}$ = 17.5 kcal·mol^{-1}), which we consider as providing significant support for the suggested model of the reaction mechanism. We would like to stress that the mechanism presented here represents the least energy pathway found among numerous structures and potential pathways studied (several of them are compiled in the Supporting Information).

DISCUSSION

This study aimed to characterize the reaction cycle of human glutamate carboxypeptidase II by a joint experimental and theoretical effort. The X-ray structure of the substrate bound in the active site of the GCPII(E424A) mutant with an intact, planar peptide bond suggests that Glu424 is directly involved in enzyme-catalyzed substrate

hydrolysis. Previously, Glu424 was subjected to site-directed mutagenesis by Speno and co-workers (*22*). In their study, Glu424 was mutated to glutamine, and the resulting E424Q mutant was characterized by an approximately 7-fold lower substrate turnover and a 2-fold higher Michaelis constant compared to the wild-type enzyme using crude cell membrane preparations. Our preliminary results, obtained with purified proteins, indicate that the activity of the GCPII(E424Q) mutant is even lower, by at least 3 orders of magnitude compared to the wild-type GCPII (data not shown). These experimental observations are qualitatively reflected by the presented theoretical calculations carried out for the wild-type GCPII. This fact, in turn, provides an indirect support for our structural model (QM/MM) of transition state. Our calculations suggest that the residual hydrolytic activity of the E424Q mutant is not totally unexpected, since a glutamine residue can be involved in the same type of interactions as the protonated glutamate. Hence, the rate-determining step in the case of E424Q may not be the formation of the tetrahedral intermediate, but likely a proton transfer reaction that involves intermediates and/or transition states that are higher in energy than in the native enzyme.

It is worth noting that in crystal structures of the complexes between wild-type GCPII and *gem*-diolate transition state mimetics (*20*,*21*) the distance between the active site Zn^{2+} ions increases by ~0.4 Å (as compared to the Michaelis complex), and this motion is assisted by a shift of the side chains of His377 and His553 (Figure S2, Supporting Information). Similar distance variability of Zn^{2+} has been noted during the reaction cycle of AAP, and it has been suggested that positional flexibility of metal ions is required as a response to a constantly changing environment in the active site of binuclear enzymes (*24*). This phenomenon is reproduced by the QM/MM calculations of the transition state structure, which predict an increase in Zn−Zn distance of ~0.2 Å, providing additional validation of the proposed mechanism.

The Zn1 ion, coordinated by the side chains of Asp387, Glu425, and His553, serves as a catalytic metal by polarizing the carbon−oxygen bond of the substrate [R(Zn−O) = 2.3 Å in the transition state]. The polarization and positioning of the substrate carbonyl are further assisted by its interactions with the Tyr552 hydroxyl group (2.6 Å). Contacts between Tyr552 and the *N*-Ac-Asp-Glu carbonyl oxygen as well as the oxygen of transition state mimetics suggest that Tyr552 is important for substrate orientation and stabilization during the GCPII reaction cycle. This conclusion is corroborated by mutagenesis data showing that mutation of Tyr552 has a profound effect on the catalytic efficiency of the enzyme (*23*) and is also in line with findings reported by Fundoiano-Hershcovitz and co-workers for the *S. griseus* aminopeptidase (*46*). The hydroxyl group of Tyr552 is concomitantly polarized by its interaction with Arg210 (see Figure 2), which further enhances the strength of interaction between Tyr552 and the substrate/transition state.

The Zn2 ion, coordinated by the side chains of His377, Asp387, and Asp453, does not directly interact with the substrate. The QM/MM equilibrium structures with the substrate acetyl oxygen bound to Zn2 (see Figures S6, S7) showed neither the enhanced stability nor lowered activation barriers. The Zn2 ion rather seems to play an important role in positioning the OH^- moiety away from the proton on Glu424 and assists in proper orientation and stabilization of the tetrahedral transition state (*20*) and can be viewed as a cocatalytic ion in analogy to the cocatalytic metals found in other dizinc hydrolases (*2*−*4*).

The Reaction Mechanism. The OH^- anion that is coordinated between two Zn^{2+} ions in the GCPII active site is considerably less nucleophilic than a free hydroxide ion, as two of its lone pairs are engaged in coordination bonds to the zinc ions. Consequently, the QM/MM calculations indicate that a direct nucleophilic attack of the hydroxide on the peptide bond carbon is an unlikely alternative. The reaction is more likely to proceed concertedly with the proton approaching the peptide bond nitrogen atom, leading to its pyramidalization and concomitant formation of a metastable tetrahedral intermediate. Glu424 acts as a general base/acid, shuttling the first proton from the activated water molecule to the peptide bond nitrogen and then accepting the second proton from the bridging hydroxide anion (which is becoming the carboxylate oxygen during the reaction). The key features are the availability of the proton separated from the activated water, the flexibility of the Glu424 residue, on which the proton resides, and the position of the Gly518 carbonyl group stabilizing both the electrophilic hydroxyl group of Glu424 and the scissile peptide bond nitrogen in close proximity.

In simple terms, we propose to describe the *N*-Ac-Asp-Glu hydrolysis by GCPII as the reaction between a *deactivated* hydroxide with an *activated* peptide bond assisted by glutamate as a general acid/base. Crossing the first barrier of the reaction may be considered as the stabilization of the less populated resonance structure of the peptide bond (−NH−C^+−O^- vs more stable −NH−C=O−) via its proximity to the Zn1 ion and its interaction with the Tyr552 hydroxyl group. Essentially, the peptide bond nitrogen must be stabilized in the sp^3 hybridization state via interaction with the proton on the carboxylic group of Glu424. As a result, the electrophilicity of the peptide carbon is increased, thus facilitating the formation of a bond between the carbon and the oxygen from the OH^- ion. A crossing of the second barrier is triggered by a proton transfer from the protonated Glu424 to the nitrogen of the peptide bond. This first proton transfer is followed by a second shift of the proton from the OH^- moiety, already bound to the peptide bond carbon to Glu424. At the same time the peptide bond is cleaved.

The architectures of the GCPII catalytic site and the metal-binding residues are similar to those of other dizinc metallopeptidases. The aminopeptidases from *Aeromonas proteolytica* (AAP) and *Streptomyces griseus* (SGAP) have the same metal-binding residues as GCPII. Although bovine lens leucine aminopeptidase (blLAP) and *Escherichia coli* aminopeptidase A (PepA) have different zinc-coordinating residues, their relative spatial arrangement is quite similar to that found in GCPII (Figure 6).

In our view, the essential feature of the hydrolysis catalyzed by GCPII is a "productive" orientation of the

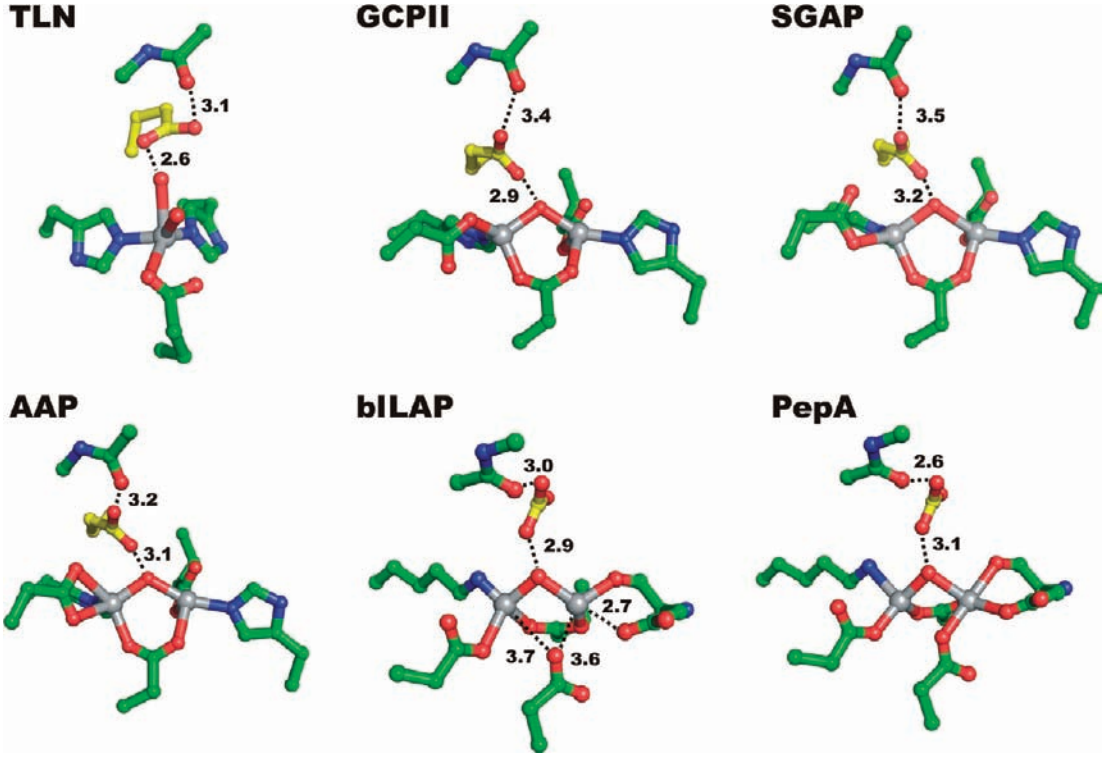

FIGURE 6: Comparison of unoccupied active sites of various metallopeptidases: TLN, *Bacillus thermoproteolyticus* thermolysin (PBD code 1LNF); GCPII, human glutamate carboxypeptidase II (PDB code 2OOT); SGAP, *S. griseus* aminopeptidase (PDB code 1CP7); AAP, *A. proteolytica* aminopeptidase (PDB code 1RTQ); blLAP, bovine lens leucine aminopeptidase (PDB code 1LAM); PepA, *E. coli* aminopeptidase A (PDB code 1GYT). Zinc ions are in gray and carbon atoms in green; the putative proton shuttles are highlighted by carbons in yellow.

Glu424 side chain, which is stabilized by the interaction with the backbone carbonyl oxygen of Gly518 (Figure 3). Such an "active conformation" of Glu424 seems to be crucial in order for the reaction to proceed. Interestingly, this conformation is present in the crystal structure of free GCPII (*18*). A similar pattern of Glu−carbonyl interactions is observed in structures of the above-mentioned aminopeptidases (*24*,*47*−*49*) (Figure 6). The presence of glutamate as a second shell residue and its putative catalytic role as a proton shuttle have been proposed previously for thermolysin by Monzingo and Matthews (*50*). Thus, we can hypothesize that the reaction mechanisms of these enzymes have a common pattern characterized by cooperation between a protonated glutamate residue, which accommodates and shuttles the proton from the activated water molecule, and a backbone carbonyl group (Gly518 in the case of GCPII) of an enzyme. The latter is not only hydrogen bonded to the protonated glutamate but at the same time also forms a hydrogen bond to the amide group of the scissile peptide bond of the substrate, assisting in a "productive orientation" of the latter.

CONCLUSIONS

In this study, we present crystallographic, biochemical, and computational evidence that allows us to propose a detailed reaction mechanism of substrate hydrolysis by human glutamate carboxypeptidase II. The crystal structure of the substrate bound in the active site of the GCPII (E424A) mutant is the first experimental description of a GCPII Michaelis complex. Using the QM/MM approach we identified the intermediate and the two transition states and suggested the complete reaction cycle. Its hallmark is the concerted nucleophilic attack of the bridging hydroxide moiety together with the electrophilic attack of a proton bound to Glu424, which results in the pyramidalization of the peptide bond nitrogen and the formation of the tetrahedral intermediate. Our experimental and theoretical data on the GCPII reaction mechanism are consistent with findings of others on related aminopeptidases (*2*,*24*−*26*) and suggest a common mechanism of substrate hydrolysis by this class of enzymes.

ACKNOWLEDGMENT

The authors thank Hillary Hoffman for language corrections. We are grateful for use of the 22-BM beamline of the Southeast Regional Collaborative Access Team (SER-CAT) located at the Advanced Photon Source (APS), Argonne National Laboratory.

SUPPORTING INFORMATION AVAILABLE

Equilibrium geometries of all molecules studied (or QM regions in the case of QM/MM calculations) and complete coordinates of the initial protein structure used as the model throughout this work (in PDB format). This material is available free of charge via the Internet at http://pubs.acs.org.

REFERENCES

1. Cauwe, B., Van den Steen, P. E., and Opdenakker, G. (2007) The biochemical, biological, and pathological kaleidoscope of cell surface substrates processed by matrix metalloproteinases. *Crit. Rev. Biochem. Mol. Biol. 42*, 113–185.

2. Holz, R. C., Bzymek, K. P., and Swierczek, S. I. (2003) Co-catalytic metallopeptidases as pharmaceutical targets. *Curr. Opin. Chem. Biol. 7*, 197–206.
3. Holz, R. C. (2002) The aminopeptidase from *Aeromonas proteolytica*: structure and mechanism of co-catalytic metal centers involved in peptide hydrolysis. *Coord. Chem. Rev. 232*, 5–26.
4. Lowther, W. T., and Matthews, B. W. (2002) Metalloaminopeptidases: Common functional themes in disparate structural surroundings. *Chem. Rev. 102*, 4581–4608.
5. Wouters, M. A., and Husain, A. (2001) Changes in zinc ligation promote remodeling of the active site in the zinc hydrolase superfamily. *J. Mol. Biol. 314*, 1191–1207.
6. Rawlings, N. D., and Barrett, A. J. (1997) Structure of membrane glutamate carboxypeptidase. *Biochim. Biophys. Acta 1339*, 247–252.
7. Chevrier, B., Schalk, C., D'Orchymont, H., Rondeau, J. M., Moras, D., and Tarnus, C. (1994) Crystal structure of *Aeromonas proteolytica* aminopeptidase: a prototypical member of the co-catalytic zinc enzyme family. *Structure 2*, 283–291.
8. Greenblatt, H. M., Almog, O., Maras, B., Spungin-Bialik, A., Barra, D., Blumberg, S., and Shoham, G. (1997) *Streptomyces griseus* aminopeptidase: X-ray crystallographic structure at 1.75 Å resolution. *J. Mol. Biol. 265*, 620–636.
9. Kinoshita, Y., Kuratsukuri, K., Landas, S., Imaida, K., Rovito, P. M.Jr., Wang, C. Y., and Haas, G. P. (2006) Expression of prostate-specific membrane antigen in normal and malignant human tissues. *World J. Surg. 30*, 628–636.
10. Troyer, J. K., Beckett, M. L., and Wright, G. L.Jr. (1995) Detection and characterization of the prostate-specific membrane antigen (PSMA) in tissue extracts and body fluids. *Int. J. Cancer 62* 552–558.
11. Šácha, P., Zámečník, J., Bařinka, C, Hlouchová, K., Vícha, A., Mlčochová, P., Hilgert, I., Eckschlager, T., and Konvalinka, J. (2007) Expression of glutamate carboxypeptidase II in human brain. *Neuroscience 144*, 1361–1372.
12. Robinson, M. B., Blakely, R. D., Couto, R., and Coyle, J. T. (1987) Hydrolysis of the brain dipeptide N-acetyl-L-aspartyl-L-glutamate. Identification and characterization of a novel N-acetylated alpha-linked acidic dipeptidase activity from rat brain. *J. Biol. Chem. 262*, 14498–14506.
13. Pinto, J. T., Suffoletto, B. P., Berzin, T. M., Qiao, C. H., Lin, S., Tong, W. P., May, F., Mukherjee, B., and Heston, W. D. (1996) Prostate-specific membrane antigen: a novel folate hydrolase in human prostatic carcinoma cells. *Clin. Cancer Res. 2*, 1445–1451.
14. Slusher, B. S., Vornov, J. J., Thomas, A. G., Hurn, P. D., Harukuni, I., Bhardwaj, A., Traystman, R. J., Robinson, M. B., Britton, P., Lu, X. C., Tortella, F. C., Wozniak, K. M., Yudkoff, M., Potter, B. M., and Jackson, P. F. (1999) Selective inhibition of NAALADase, which converts NAAG to glutamate, reduces ischemic brain injury. *Nat. Med. 5*, 1396–1402.
15. Zhou, J., Neale, J. H., Pomper, M. G., and Kozikowski, A. P. (2005) NAAG peptidase inhibitors and their potential for diagnosis and therapy. *Nat. Rev. Drug Discov. 4*, 1015–1026.
16. Gong, M. C., Chang, S. S., Sadelain, M., Bander, N. H., and Heston, W. D. (1999) Prostate-specific membrane antigen (PSMA)-specific monoclonal antibodies in the treatment of prostate and other cancers. *Cancer Metastasis Rev. 18*, 483–490.
17. Davis, M. I., Bennett, M. J., Thomas, L. M., and Bjorkman, P. J. (2005) Crystal structure of prostate-specific membrane antigen, a tumor marker and peptidase. *Proc. Natl. Acad. Sci. U.S.A. 102*, 5981–5986.
18. Bařinka, C., Starková, J., Konvalinka, J., and Lubkowski, J. (2007) A high-resolution structure of ligand-free human glutamate carboxypeptidase II. *Acta Crystallogr., Sect. F: Struct. Biol. Cryst. Commun. 63*, 150–153.
19. Mesters, J. R., Bařinka, C., Li, W., Tsukamoto, T., Majer, P., Slusher, B. S., Konvalinka, J., and Hilgenfeld, R. (2006) Structure of glutamate carboxypeptidase II, a drug target in neuronal damage and prostate cancer. *EMBO J. 25*, 1375–1384.
20. Bařinka, C., Hlouchová, K., Rovenská, M., Majer, P., Dauter, M., Hin, N., Ko, Y., Tsukamoto, T., Slusher, B. S., Konvalinka, J., and Lubkowski, J. (2008) Structural basis of interactions between human glutamate carboxypeptidase II and its substrate analogs. *J. Mol. Biol. 376*, 1438–1450.
21. Bařinka, C., Rovenská, M., Mlčochová, P., Hlouchová, K., Plechanovová, A., Majer, P., Tsukamoto, T., Slusher, B. S., Konvalinka, J., and Lubkowski, J. (2007) Structural insight into the pharmacophore pocket of human glutamate carboxypeptidase II. *J. Med. Chem. 50*, 3267–3273.
22. Speno, H. S., Luthi-Carter, R., Macias, W. L., Valentine, S. L., Joshi, A. R., and Coyle, J. T. (1999) Site-directed mutagenesis of predicted active site residues in glutamate carboxypeptidase II. *Mol. Pharmacol. 55*, 179–185.
23. Mlčochová, P., Plechanovová, A., Bařinka, C., Mahadevan, D., Saldanha, J. W., Rulíšek, L., and Konvalinka, J. (2007) Mapping of the active site of glutamate carboxypeptidase II by site-directed mutagenesis. *FEBS J. 274*, 4731–4741.
24. Desmarais, W., Bienvenue, D. L., Bzymek, K. P., Petsko, G. A., Ringe, D., and Holz, R. C. (2006) The high-resolution structures of the neutral and the low pH crystals of aminopeptidase from *Aeromonas proteolytica*. *J. Biol. Inorg. Chem. 11*, 398–408.
25. Schürer, G., Horn, A. H. C., Gedeck, P., and Clark, T. (2002) The reaction mechanism of bovine lens leucine aminopeptidase. *J. Phys. Chem. B 106*, 8815–8830.
26. Chen, S., Marino, T., Fang, W., Russo, N., and Himo, F. (2008) Peptide hydrolysis by the binuclear zinc enzyme aminopeptidase from *Aeromonas proteolytica*: A density functional theory study *J. Phys. Chem. B 112*, 2494–2500.
27. Bařinka, C., Rinnová, M., Šácha, P., Rojas, C., Majer, P., Slusher, B. S., and Konvalinka, J. (2002) Substrate specificity, inhibition and enzymological analysis of recombinant human glutamate carboxypeptidase II. *J. Neurochem. 80*, 477–487.
28. Otwinowski, Z., and Minor, W.(1997) Processing of X-ray diffraction data collected in oscillation mode, in *Methods in Enzymology* (Carter, C. W., Jr., and Sweet, R. M., Eds.) pp 307−326, Academic Press, New York..
29. Murshudov, G. N., Vagin, A. A., Lebedev, A., Wilson, K. S., and Dodson, E. J. (1999) Efficient anisotropic refinement of macromolecular structures using FFT. *Acta Crystallogr., Sect. D: Biol. Crystallogr. 55*, 247–255.
30. McRee, D. E. (1999) XtalView/Xfit—A versatile program for manipulating atomic coordinates and electron density. *J. Struct. Biol. 125*, 156–165.
31. Laskowski, R. A., McArthur, M. W., Moss, D. S., and Thornton, J. M. (1993) PROCHECK: a program to check the stereochemical quality of protein structures. *J. Appl. Crystallogr. 26*, 283–291.
32. Ryde, U. (1996) The coordination of the catalytic zinc ion in alcohol dehydrogenase studied by combined quantum chemical and molecular mechanical calculations. *J. Comput.-Aided Mol. Des. 10* 153–164.
33. Treutler, O., and Ahlrichs, R. (1995) Efficient molecular numerical integration schemes. *J. Chem. Phys. 102*, 346–354.
34. Cornell, W. D., Cieplak, P., Bayly, C. I., Gould, I. R., Merz, K. M., Ferguson, D. M., Spellmeyer, D. C., Fox, T., Caldwell, J. W., and Kolman, P. A. (1995) Second generation force field for the simulation of proteins, nucleic acids and organic molecules. *J. Am. Chem. Soc. 117*, 5179–5197.
35. Perdew, J. P., Burke, K., and Ernzerhof, M. (1996) Generalized gradient approximation made simple. *Phys. Rev. Lett. 77* 3865–3868.
36. Eichkorn, K., Weigen, F., Treutler, O., and Ahlrichs, R. (1997) Auxiliary basis sets for main row atoms and transition metals and their use to approximate Coulomb potentials. *Theor. Chim. Acta 97*, 119–124.
37. Weigend, F., and Ahlrichs, R. (2005) Balanced basis sets of split valence, triple-ζ valence and quadruple-ζ valence quality for H to Rn: design and assessment of accuracy. *Phys. Chem. Chem. Phys. 7*, 3297–3305.
38. Becke, A. D. (1993) Density-functional thermochemistry. III. The role of exact exchange. *J. Chem. Phys. 98*, 5648–5652.
39. Woon, D. E., and Dunning, T. H.Jr. (1993) Gaussian basis sets for use in correlated molecular calculations. III. The atoms aluminum through argon. *J. Chem. Phys. 98*, 1358–1371.
40. Kendall, R. A., Dunning, T. H.Jr., and Harrison, R. J. (1992) Electron affinities of the first-row atoms revisited. Systematic basis sets and wave functions. *J. Chem. Phys. 96*, 6796–6806.
41. Schäfer, A., Klamt, A., Sattel, D., Lohrenz, J. C. W., and Eckert, F. (2000) COSMO Implementation in TURBOMOLE: Extension of an efficient quantum chemical code towards liquid systems. *Phys. Chem. Chem. Phys. 2*, 2187–2193.
42. Harding, M. M. (1999) The geometry of metal−ligand interactions relevant to proteins. *Acta Crystallogr., Sect. D: Biol. Crystallogr. 55*, 1432–1443.
43. Diaz, N., Suarez, D., and Merz, K. M.Jr. (2000) Zinc metallo-β-lactamase from *Bacteroides fragilis*: a quantum chemical study on model systems of the active site. *J. Am. Chem. Soc. 122*, 4197–4208.
44. Stamper, C., Bennett, B., Edwards, T., Holz, R. C., Ringe, D., and Petsko, G. (2001) Inhibition of the aminopeptidase from Aeromonas

proteolytica by L-leucinephosphonic acid. Spectroscopic and crystallographic characterization of the transition state of peptide hydrolysis. *Biochemistry 40*, 7035–7046.
45. Schürer, G., Lanig, H., and Clark, T. (2004) Aeromonas proteolytica aminopeptidase: an investigation of the mode of action using a QM/MM approach. *Biochemistry 43*, 5414–5427.
46. Fundoiano-Hershcovitz, Y., Rabinovitch, L., Langut, Y., Reiland, V., Shoham, G., and Shoham, Y. (2004) Identification of the catalytic residues in the double-zinc aminopeptidase from *Streptomyces griseus*. *FEBS Lett. 571*, 192–196.
47. Gilboa, R., Greenblatt, H. M., Perach, M., Spungin-Bialik, A., Lessel, U., Wohlfahrt, G., Schomburg, D., Blumberg, S., and Shoham, G. (2000) Interactions of *Streptomyces griseus* aminopeptidase with a methionine product analogue: a structural study at 1.53 Å resolution. *Acta Crystallogr., Sect. D: Biol. Crystallogr. 56*, 551–558.
48. Strater, N., and Lipscomb, W. N. (1995) Two-metal mechanism of bovine lens leucine aminopeptidase: active site solvent structure and binding mode of L-leucinal, a gem-diolate transition state analogue, by X-ray crystallography. *Biochemistry 34*, 14792–14800.
49. Strater, N., Sherratt, D. J., and Colloms, S. D. (1999) X-ray structure of aminopeptidase A from *Escherichia coli* and a model for the nucleoprotein complex in Xer site-specific recombination. *EMBO J. 18*, 4513–4522.
50. Monzingo, A. F., and Matthews, B. W. (1984) Binding of N-carboxymethyl dipeptide inhibitors to thermolysin determined by X-ray crystallography: a novel class of transition-state analogs for zinc peptidases. *Biochemistry 23*, 5724–5729.